Lead-Free Organic-Inorganic Tin Halide Perovskites for Photovoltaic Applications

Nakita K. Noel,[1] Samuel D. Stranks,[1] Antonio Abate,[1] Christian Wehrenfennig,[1] Simone Guarnera,[2,3] Amir-Abbas Haghighirad,[1] Aditya Sadhanala,[4] Giles E. Eperon,[1] Sandeep K. Pathak,[1] Michael B. Johnston,[1] Annamaria Petrozza,[2] Laura M. Herz,[1] Henry J. Snaith[1*]

[1] Clarendon Laboratory, Department of Physics, University of Oxford, Parks Road, Oxford, OX1 3PU, United Kingdom

[2] Centre for Nano Science and Technology@PoliMi, Instituto Italiano di Tecnologia, Via Giovanni Pascoli 70/3, 20133 Milano, Italy

[3] Dipartimento di Fisica, Politecnico di Milano, Piazza L. da Vinci 32, 20133 Milano, Italy

[4] Cavendish Laboratory, Department of Physics, University of Cambridge, 19 JJ Thomson Ave, Cambridge, CB3 0HE, United Kingdom

*Corresponding author: Henry J. Snaith, e-mail: h.snaith1@physics.ox.ac.uk

SUPPORTING INFORMATION

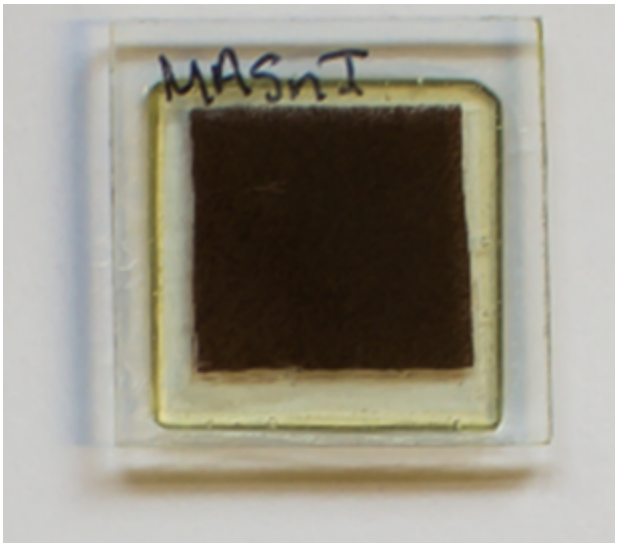

Figure S1- Photograph showing a film of the black/brown, $CH_3NH_3SnI_3$. This film was sealed in a nitrogen filled glove box and has been aged for 4 months under AM1.5 76mWcm^{-2} sun light generated from a sun-test CPSPlus light soaking box.

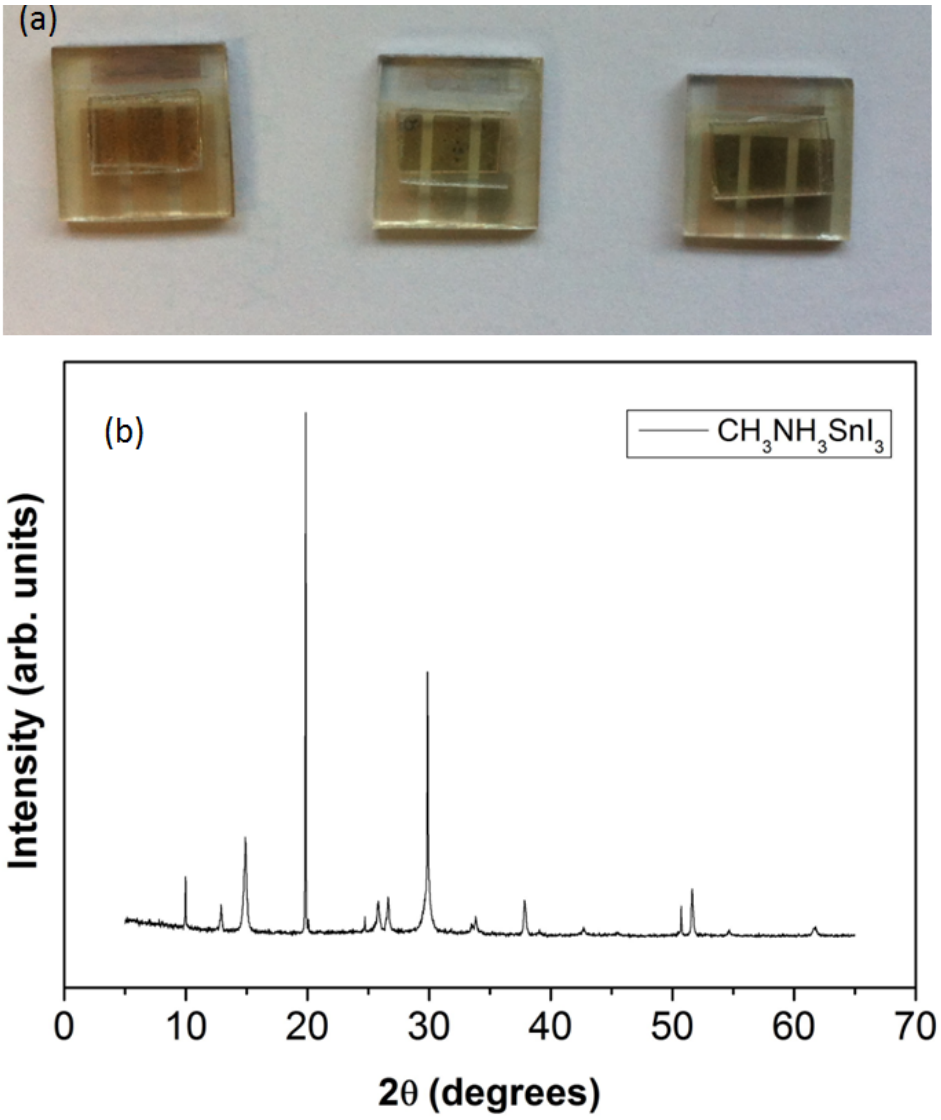

Figure S2: (a) Photograph showing solar cell devices where the $CH_3NH_3SnI_3$ absorber layer has degraded. **(b)** X-ray Diffractogram of a degraded sample of $CH_3NH_3SnI_3$.

X-ray Diffraction

The X-ray diffraction pattern shown above corresponds to methylammonium iodide with some impurities. The lattice parameters derived were as follows: a= 11.2246 Å and c= 8.9362 Å.

While we note that there are no visible peaks for any oxides of tin, this is quite likely due to the formation of amorphous species which will not be clearly detected by this measurement.

Scanning Electron Microscopy (SEM) Images

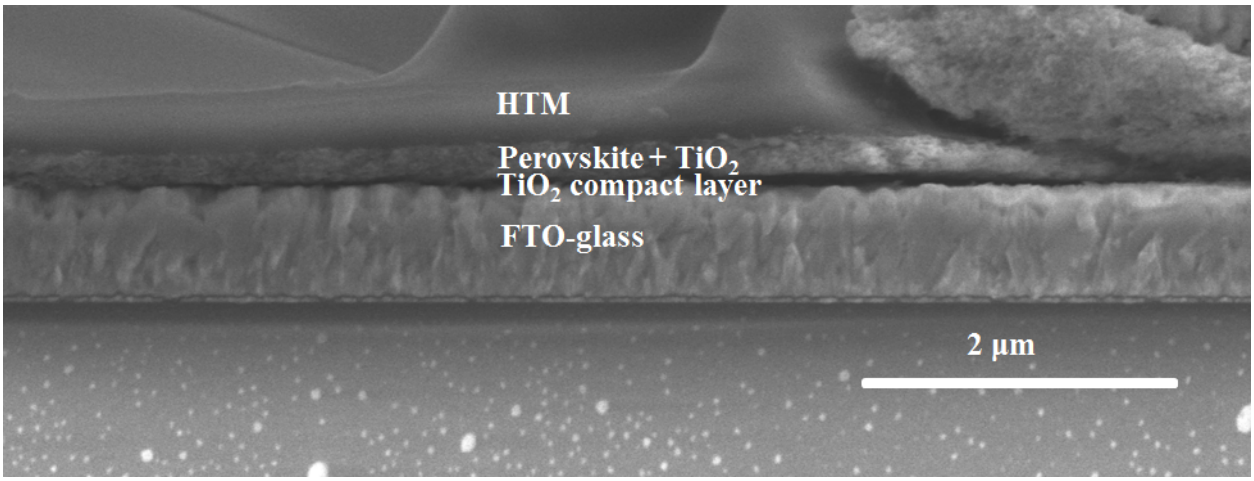

Figure S3: Cross-Sectional Scanning Electron Microscope (SEM) Image. Cross-sectional SEM image of a TiO_2-based $CH_3NH_3SnI_3$ device.

The cross-sectional SEM image above shows clearly that there is no capping layer of perovskite formed by $CH_3NH_3SnI_3$ in this device configuration. In a device with a 400 nm thick mesoporous TiO_2, the perovskite material is contained solely within the pores of the TiO_2. The delamination of the TiO_2 layer is as a result of fracturing the device. The formation of a capping layer in such a device is undesirable as a result of the short diffusion length of the material, which will cause recombination to occur on a faster timescale than charge extraction. Top view images of both 80 nm thick and 400 nm thick TiO_2 films infiltrated with $CH_3NH_3SnI_3$ are shown

below. This image very accurately illustrates the loss of the capping layer with increased film thickness.

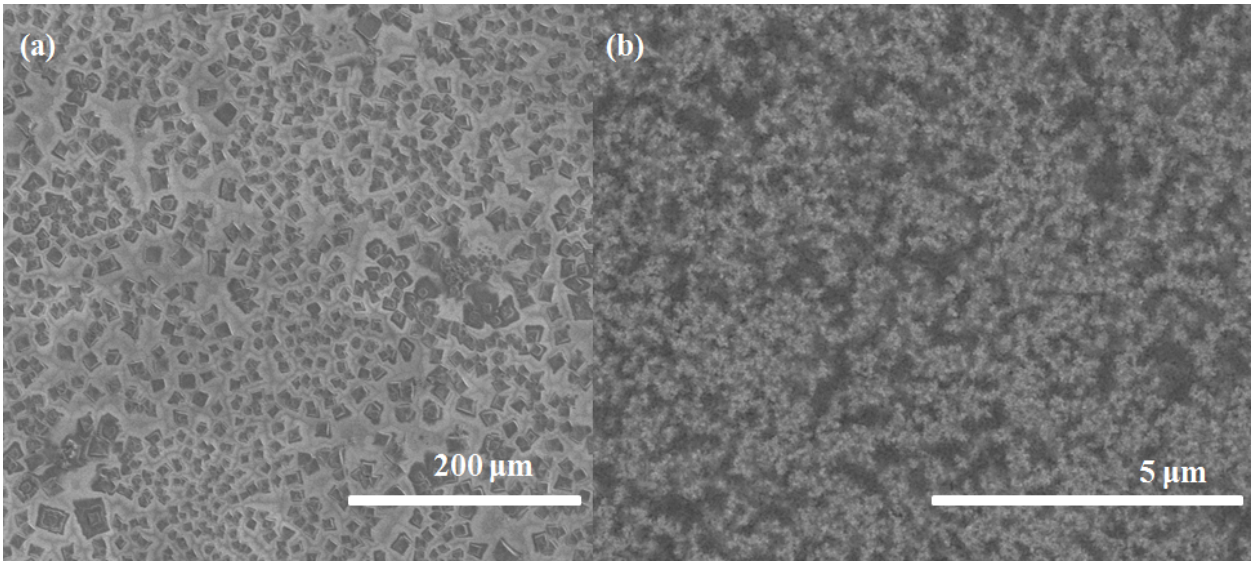

Figure S4: Top-View Scanning Electron Microscope Images. Top view SEM image of (a) A capping layer of disperse $CH_3NH_3SnI_3$ crystal formed on an 80 nm thick film of TiO_2. (b) $CH_3NH_3SnI_3$ coated on a 400 nm thick film of TiO_2 such that all of the crystallites have formed within the pores of the TiO_2 and no capping layer is present.

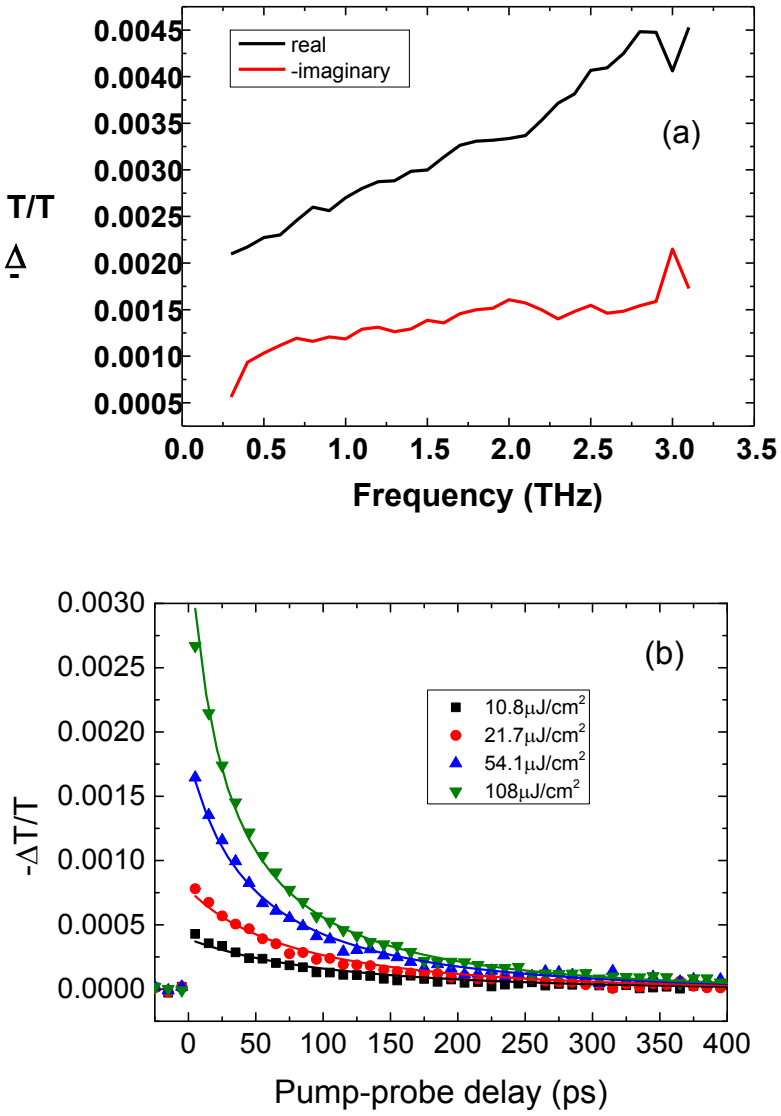

Figure S3: Terahertz spectroscopy. (a) Terahertz photo induced absorption spectrum (obtained through inverse Fourier Transform of the time-domain response ΔT(t)/T(t)) for a sample of $CH_3NH_3SnI_3$ on 80-nm thick mesoporous TiO_2 (excitation wavelength: 550 nm, fluence 108 μJ cm^{-2}). (b) Transient terahertz photoconductivity of $CH_3NH_3SnI_3$ on 80-nm thick mesoporous Al_2O_3 at a range of excitation fluences (excitation wavelength: 550 nm). Symbols represent experimental data while solid lines are fits to the data using the model described in the

text. We extract an effective free carrier mobility of $\varphi\mu$ = 1.58 $cm^2 V^{-1} s^{-1}$, a bimolecular rate constant of $\varphi\gamma$ = 1.01 x10^{-9} $cm^3 s^{-1}$, and hole-doping density of p_0 = 6.39 x10^{18} cm^{-3}

THz Time-Domain Spectroscopy

Figure S3a shows the frequency-spectrum of the complex photoinduced THz conductivity recorded at a pump-probe delay of 20 ps. We note that no change in the spectral shape with time is observed and hence the data shown are representative of the entire investigated timescale. The spectrum can clearly not be described by a simple Drude-like free-carrier response. The data are however consistent with the THz conductivity of free carriers in the presence of localization effects, such as those arising from backscattering at crystallite boundaries (1). A similar spectral response to the one observed here has e.g. been found in sintered TiO_2 nanoparticle films (1) (2). While an excitonic resonance would be able to explain the rise in the real part of the THz spectrum towards higher frequencies, it is not consistent with a non-zero imaginary part at low-freqencies. Hall measurements on $CH_3NH_3SnI_3$ have revealed about eight times higher mobilities for electrons than for holes; therefore we expect that the transient THz response due to photoexcited carriers is dominated by free electrons (3).

Derivation of photoconductivity and charge carrier mobility from the change in THz electric field transmission

The sheet photoconductivity ΔS of a thin film between two media of refractive indices n_A and n_B, under the condition that the thickness of the film is much smaller than the THz wavelength, may be expressed as (4) (5)

$$\Delta S = -\epsilon_0 c(n_A + n_B)\left(\frac{\Delta T}{T}\right), \qquad (1)$$

where $\Delta T = T_{\text{illuminated}} - T$ is the photoinduced change in terahertz electric field. Here, T and $T_{\text{illuminated}}$ are the transmitted terahertz electric fields of the sample in the dark and after photoexcitation respectively. In our experiment the sample film is surrounded by vacuum from one side, hence $n_A = 1$ and in contact with the z-cut quartz substrate with THz-refractive index $n_B = 2.13$ from the other side.

In order to derive the charge-carrier mobility μ from the photoinduced sheet conductivity, the number of photo-excited charge carriers N needs to be determined using

$$N = \varphi \frac{E\lambda}{hc}(1 - R_{\text{pump}})(1 - T_{\text{pump}}) \qquad (2)$$

Here, E is the energy contained in an optical excitation pulse of wavelength λ, R_{pump} is the reflectivity of the sample at normal incidence of the excitation beam, T_{pump} the (small) fraction of light transmitted through the sample and φ is the ratio of free charge carriers created per photons absorbed, commonly referred to as the photon-to-charge branching ratio, which is technically undetermined in the experiment and related to factors such as the exciton binding energy in the material. We argue however in the main manuscript that there is some evidence making it appear likely that φ is not substantially lower than unity.

The charge carrier mobility μ is given by

$$\mu = \frac{\Delta S \, A_{\text{eff}}}{Ne} \qquad (3)$$

where A_{eff} is the effective area of the overlap of optical pump and THz probe pulse taking into account the Gaussian beam profiles, and e is the elementary charge. With φ unknown, the quantity which can be directly derived from the experiment is the effective mobility $\tilde{\mu} = \varphi\mu$ where

$$\varphi\mu = -\varepsilon_0 c(n_A + n_B)\frac{A_{\text{eff}}\, hc}{E\, e\, \lambda\, (1 - R_{\text{pump}})(1 - T_{\text{pump}})}\left(\frac{\Delta T}{T}\right) \qquad (4)$$

Because $0 \leq \varphi \leq 1$, the effective mobility represents a lower limit, which becomes identical to the actual mobility for full photon-to-free-carrier conversion. The determined charge carrier mobility arises from the contributions of both electrons and holes, which cannot be separated. Therefore the extracted mobility value is the sum of electron and hole mobilities.

To allow accurate determination of $\varphi\mu$ we ensured that excitation conditions are in the linear regime. We have evaluated the dependence of the initial amplitude of the THz response on excitation fluence and found that nonlinear processes such as two-photon absorption do not have significant effect in the range of fluences used in this study (≤ 110 μJ cm^{-2}).

Fits to THz photoconductivity transients

As described in the main manuscript, we model the decay dynamics of the photoexcited electron density $n(t)$ in terms of recombination with photoexcited and doped holes ($p(t) + p_0$). We neglect the influence of mono-molecular contributions from trap-mediated processes as well as third- or higher order processes. The former assumption can to some extent be justified from the comparison to the related lead halide materials, where trap-induced effects have been found to occur on timescales more than two orders of magnitude longer than those studies in our THz experiments (6) (7) (8). This results in the following rate equation:

$$\frac{dn}{dt} = -\gamma n(p + p_0) = -\gamma np - \gamma np_0 \qquad (5)$$

Here, γ is the electron-hole recombination rate constant. Note that, since (after thermalization) photoinduced and doped holes are indistinguishable, the corresponding population is described in terms of the sum of the initial hole density before photoexcitation p_0 and the dynamic contribution p(t). In this definition p_0 is equal to the doped hole density in the absence of illumination and $p(0)$ the initial photoexcited hole density (before any recombination events). Since our model only allows decay via e-h-recombination events, n and p have to follow the same time-evolution. As furthermore $n(0) = p(0)$, it follows that n(t) = p(t) and therefore (5) becomes

$$\frac{dn}{dt} = -\gamma n^2 - \gamma p_0 n = -k_2 n^2 - k_1 n \qquad (6)$$

with $k_2 \stackrel{\text{def}}{=} \gamma$ and $k_1 \stackrel{\text{def}}{=} \gamma p_0$. The experimentally observed quantity is the photoinduced THz transmission change $x(t) \stackrel{\text{def}}{=} (\Delta T/T)(t)$, which is linearly related to the free carrier density (see (1) and (3)):

$$n(t) = \varphi\, C\, x(t)\,. \qquad (7)$$

Here $C = \tilde{n}_0/x(0)$ is the proportionality factor between the immediate THz response $x(0)$ and the absorbed photon density

$$\tilde{n}_0 = \frac{E\lambda\, \alpha(\lambda)}{hc\, A_{\text{eff}}}\left(1 - R_{\text{pump}}\right), \qquad (8)$$

which can be calculated from the pump beam parameters and the absorption coefficient of the sample α at the excitation wavelength λ.

Substituting (7) into (5) we obtain

$$\frac{dx}{dt} = -C\varphi k_2 x^2 - k_1 x \qquad (9)$$

$$= -A_2 x^2 - A_1 x$$

with $A_2 = C\varphi k_2 = C\varphi\gamma$ and $A_1 = k_1 = \gamma p_0$. We fit solutions to this equation simultaneously to all acquired THz transients of a fluence-dependent set (i.e. there is only one globally optimized value for each of the two rate constants A_1 and A_2, which is applied to all fluences). As the photon-to-free-carrier conversion ratio φ is unknown, we can, strictly speaking, only determine the values $\varphi\gamma = A_2/C$ and $\varphi^{-1} p_0 = CA_1/A_2$ from our fits. These equal the actual decay rate constant γ and hole-doping density p_0 in case the material exhibits full photon-to-free-charge conversion.

To account for the spatially varying charge density profile, our fit routine takes into account the exponential charge density profile created by the pump beam by dividing the sample into 50 equally thick slabs and computing the decay function for all of these individually.

Diffusion length calculation

From the effective mobility and the recombination rate constants extracted from the THz photoconductivity transients we can calculate the charge-carrier diffusion length as follows:

$$L(n) = \sqrt{\frac{D}{R(n)}} = \sqrt{\frac{\mu\, k_B T}{e\, R(n)}} \tag{10}$$

with the D being the diffusion coefficient, T the temperature, e the electronic charge, and the R the total carrier recombination rate

$$R(n) = -\frac{1}{n}\frac{dn}{dt} = \varphi\gamma\,(n/\phi) + \gamma p_0\,. \tag{11}$$

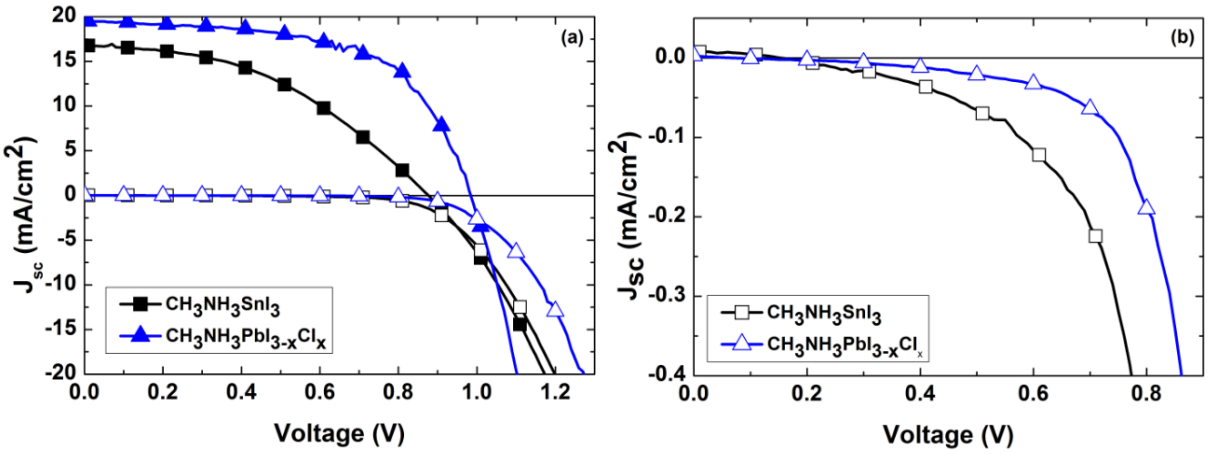

Figure S4: Current-Voltage Characteristics. (a) The current density-voltage (JV) characteristics of the best performing TiO_2 based $CH_3NH_3SnI_3$ (black) and $CH_3NH_3PbI_{3-x}Cl_x$ (blue) devices. The dark JV curves are represented by the hollow symbols. (b) A zoom in on the current scale for the dark JV curves for both devices, with $CH_3NH_3PbI_{3-x}Cl_x$ shown in blue and $CH_3NH_3SnI_3$ in black.

Leakage current

The light and dark current voltage characteristics for the best performing Pb-based and Sn-based perovskite devices fabricated on TiO_2 are show in **Figure S4**. We note here that while the leakage current of the $CH_3NH_3SnI_3$ based device is larger than the leakage current of its Pb counterpart, they are not greatly dissimilar. It is possible that in the best performing devices such as this, the background density of holes due to self-doping is lower than the hole density in other devices which show poorer performance. The uncontrolled nature of this self-doping mechanism can therefore be used to account for the large spread in the V_{oc} of a given batch, as the doping density will presumably vary from device to device. The light JV characteristics of devices with a spread of power conversion efficiencies are presented below in **Figure S5** along with the corresponding dark JV curves.

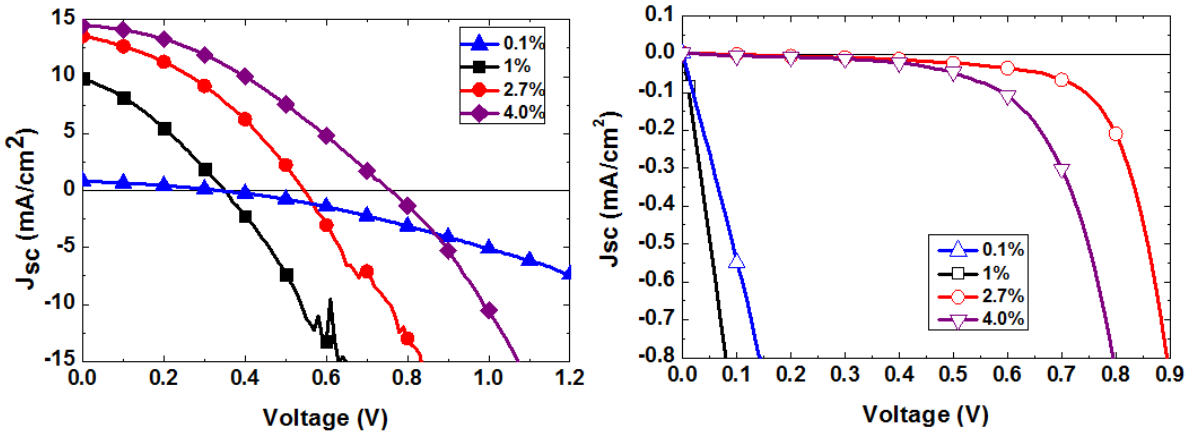

Figure S5: Current-Voltage Characteristics of Various $CH_3NH_3SnI_3$ Devices. (a) Current-voltage (JV) characteristics of $CH_3NH_3SnI_3$ devices of a spread power conversion efficiencies (PCE) under illumination. The PCEs of the devices are as follows: 0.1% (blue triangles), 1% (black squares), 2.7 % (red circles), 4.0% (purple diamonds). (b) Corresponding dark JV characteristics for the devices shown in (a), represented by hollow symbols.

The graphs above show the JV characteristics for devices with a range of power conversion efficiencies from 0.1% to 4%. In the case of the worst performing devices, we propose that the self-doping problem is so severe that it causes short-circuiting of the device. We see from the graphs presented in Figures S4 and S5 that a decrease in the doping density, and thus the leakage current of the device, corresponds to an increase in the performance of the devices. This presents strong motivation for the control of this doping mechanism, as it promises to greatly increase the efficiency of these devices.

References

1. Němec, H.; Kužel, P.; Sundström, V. Far-Infrared Response of Free Charge Carriers Localized in Semiconductor Nanoparticles. *Phys. Rev. B* **2009,** *79,* 115309.

2. Hendry, E.; Koeberg, M.; O'Regan, B.; Bonn, M. Local field effects on electron transport in nanostructured

3. Stoumpos, C. C.; Malliakas, C. D.; Kanatzidis, M. G. Semiconducting Tin and Lead Iodide Perovskites with Organic Cations: Phase Transitions, High Mobilities, and Near-Infrared Photoluminescent Properties. *Inorg. Chem.* **2013,** *52* (15), 9019-9038.

4. Nienhuys, H.-K.; Sundström, V. Intrinsic Complications in the Analysis of Optical-Pump, Terahertz Probe Experiments. *Phys. Rev. B* **2005,** *71,* 235110.

5. Ulbricht, R.; Hendry, E.; Shan, J.; Heinz, T. F.; Bonn, M. Carrier dynamics in semiconductors studied with time-resolved terahertz spectroscopy. *Rev. Mod. Phys.* **2011,** *83,* 543-586.

6. Stranks, S. D.; Eperon, G. E.; Grancini, G.; Menelaou, C.; Alcocer, M. J. P.; Leijtens, T.; Herz, L. M.; Petrozza, A.; Snaith, H. J. Electron-Hole Diffusion Lengths Exceeding 1 Micrometer in an Organometal Trihalide Perovskite Absorber. *Science* **2013,** *342* (6156), 341-344.

7. Xing, G.; Mathews, N.; Sun, S.; Lim, S. S.; Lam, Y. M.; Grätzel, M.; Mhaisalkar, S.; Sum, T. C. Long-Range Balanced Electron- and Hole-Transport Lengths in Organic-Inorganic

8. Wehrenfennig, C.; Liu, M.; Snaith, H. J.; Johnston, M. B.; Herz, L. M. Homogeneous Emission Line Broadening in the Organo Lead Halide Perovskite CH3NH3PbI3-xClx. *J. Phys. Chem. Lett.* **2014,** *5,* 1300–1306.